



**HAL**  
open science

# SeisTomoPy: Fast Visualization, Comparison, and Calculations in Global Tomographic Models

Stéphanie Durand, R Abreu, C Thomas

► **To cite this version:**

Stéphanie Durand, R Abreu, C Thomas. SeisTomoPy: Fast Visualization, Comparison, and Calculations in Global Tomographic Models. *Seismological Research Letters*, 2018, 89 (2A), pp.658-667. 10.1785/0220170142 . hal-02944870

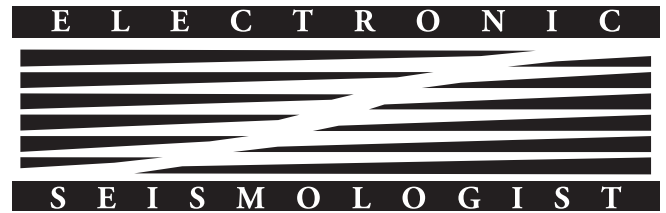
**HAL Id: hal-02944870**

**<https://hal.science/hal-02944870v1>**

Submitted on 21 Sep 2020

**HAL** is a multi-disciplinary open access archive for the deposit and dissemination of scientific research documents, whether they are published or not. The documents may come from teaching and research institutions in France or abroad, or from public or private research centers.

L'archive ouverte pluridisciplinaire **HAL**, est destinée au dépôt et à la diffusion de documents scientifiques de niveau recherche, publiés ou non, émanant des établissements d'enseignement et de recherche français ou étrangers, des laboratoires publics ou privés.



## SeisTomoPy: Fast Visualization, Comparison, and Calculations in Global Tomographic Models

by S. Durand, R. Abreu, and C. Thomas

### ABSTRACT

We present SeisTomoPy, a new Python tool that facilitates the use of a suite of tomographic models available to the public, with a single program. We placed particular emphasis on providing a tool that will be freely available on a GitHub platform and that is based on free software, Python and Fortran. SeisTomoPy provides six tools that allow the user to visualize tomographic models, compare them, and extract information for further scientific purposes. The tool comes with a graphical interface with intuitive buttons and simple parameters but the same information can also be gained using the Python classes that can be run routinely in Python scripts. This tool is suitable for global and spherical tomographic models and is provided with a default list of eight recent tomographic models. However, the users can also upload their own model if desired. By facilitating the wider use of tomographic models, SeisTomoPy aims at encouraging a wider community of geophysicists to explore tomographic models in more detail.

*Electronic Supplement:* User manual for SeisTomoPy.

### INTRODUCTION

For some time, we are facing an increase of global mantle tomographic models (e.g., Ritsema *et al.*, 2011; French and Romanowicz, 2014; Moulik and Ekström, 2014; Chang *et al.*, 2015; Simmons *et al.*, 2015; Durand *et al.*, 2016, 2017; Koelemeijer *et al.*, 2016) including both *P*- and *S*-wave models. The most recent ones are generally based on a combination of surface and body waves with or without including normal-mode data. Some of them invert surface-wave phase velocities, body-wave travel times as well as normal-mode splitting and coupling coefficients, whereas others use waveform tomographic inversions. These models are generally made public to be utilized in various studies; however, in general their formats and the places where they are stored are different, which allow neither an easy use nor the exploitation of the features within them.

In the frame of the Earth Model Collaboration (EMC) project, Incorporated Research Institutions for Seismology (IRIS) proposed to collect various models and make them available in a single format, netCDF (IRIS Data Management Center [DMC], 2011). As part of this initiative, they developed visualization tools (Hutko *et al.*, 2017), but tools for quantitatively exploiting those tomographic models are still missing.

Here we present a Python package SeisTomoPy that allows the user:

- to visualize the most recent global tomographic models, without need of reformatting, as well as models that the user would have at their disposal;
- to extract quantitative information about these models;
- to facilitate comparisons about different aspects of these models;
- to extract information for further use in other studies such as travel-time variations due to velocity changes; and
- to store the models in formats that can be used, for example, for computing synthetic seismograms for waveform modeling studies.

Our project SeisTomoPy thus provides tools that enable us to visualize, compare, and derive useful information on the most recent tomographic models, as well as on models that the user would have at their disposal. It includes both a graphical interface that makes the tool user friendly, and Python classes that can be used routinely in Python scripts.

SeisTomoPy can be used to answer scientific questions. For instance, because every tomographic model is generated with different inversion techniques, from classical ray theory (e.g., Romanowicz, 2003; Mosca and Trampert, 2009) to waveform inversion (e.g., Nolet, 1990; Stutzmann and Montagner, 1993), and is based on different datasets, it is not always easy to understand how these different approaches affect the resulting tomographic images (see Liu and Gu, 2012, for a review). Using SeisTomoPy, the comparison and analysis of effects of these different choices on imaged mantle structures are facilitated. Comparing different models may also help find a best-fitting tomographic model for other studies. Tomographic models are also often used to correct travel times for mantle heterogeneities, for example, before stacking (e.g., Schmerr and Garnero, 2006). However, extracting travel times from different tomographic models may be time consuming but with our tool we provide the possibility to compute body-wave

travel times in various tomographic models for many seismic phases in any given 2D Earth's profile in a short time. In addition, SeisTomoPy also provides input files ready to be used for computing synthetic seismograms with AxiSEM (Nissen-Meyer *et al.*, 2014). Finally, by collecting the available tomographic models, SeisTomoPy will serve as a library of available global tomographic models published after 2010 that will be regularly updated.

In the following sections, we first present the different options that are included in SeisTomoPy and the outputs that can be obtained. We then present an application of SeisTomoPy for a study where we investigate the Pacific low-velocity anomaly. We finally present future functionalities that will be added to the tool but that are beyond the scope of this first version.

## GENERAL DESCRIPTION

SeisTomoPy includes several recent tomographic models that are available to the community. They are mostly global shear velocity tomographic models, but we also include one model of the upper mantle to show that the tool can be used for a wider list of tomographic models. We will add more tomographic models as they become available, also including dedicated  $P$ -wave models and more upper-mantle models. In Table 1, we summarize the characteristics of the different models included in the first version of SeisTomoPy. For detailed information on each model, the reader is referred to the original publication.

Associated to this first library of models, we provide six tools that will aid:

- generating cross sections and extracting values of  $V_S$ ,  $V_P$ , and density as input for AxiSEM to generate synthetic seismograms;
- producing global tomographic maps at a given depth;
- computing the amplitude spectrum at any depth;
- computing the correlation at any depth between the different models;
- plotting wavepaths on the top of tomographic models; and
- computing travel times of body waves for the different tomographic models.

We will explain the usage of each of these tools below, and more details about how to use the interface and the Python classes can be found in the documentation available in the © electronic supplement to this article. A jupyter notebook tutorial is also provided to help the user become familiar with SeisTomoPy.

SeisTomoPy has been developed for saving the generated results from each of the functions in output files or figures that can be used for further scientific studies.

## MODEL FILES

### Construction

For an easy use of the different tomographic models, as detailed above, we have to convert the models into a new format that is

then used in SeisTomoPy. We decided to use spherical harmonics because it enables us to store the models in reasonable size files but still achieve fast calculations. However, this limits the use of SeisTomoPy to spherical models built using homogeneous parameterizations such as continuous functions (spherical harmonics or splines) and regular grids. Still, spherical harmonics offer a good compromise between numerical costs and the number of usable models. Using the packages that are usually distributed with the models, we create model files at every kilometer that are then decomposed in spherical harmonics up to degree 60 following

$$V(\theta, \phi, z) = \sum_{l=0}^{60} \sum_{m=-l}^l \left( \frac{\delta V}{V}(z) \right)_{lm} Y_{lm}(\theta, \phi), \quad (1)$$

in which  $V$  is the velocity at every locations  $(\theta, \phi)$  for a given depth  $z$ ,  $(\frac{\delta V}{V}(z))_{lm}$  is the spherical harmonic coefficients at every degree  $l$  and order  $m$ , and  $Y_{lm}(\theta, \phi)$  are the complex fully normalized spherical harmonics according to the definition of Edmonds (1960). Because we compute every model at every kilometer depth, we are able to capture internal discontinuities that may be included in the models such as in S362WMANI+M that includes a discontinuity at 660 km depth that is well recovered by SeisTomoPy (see Fig. 1b). We cut the spherical harmonic expansion at degree 60. It implies that for models with lower resolution, simply no energy for degrees greater than the resolution will be introduced and we verified that degree 60 is high enough to capture the complete spectrum of the included models. Unifying the models in this way also allows to filter a model below a certain harmonic degree if desired.

For the anisotropic models, we choose to represent the Voigt average which is defined for the shear velocity  $V_S^{\text{Voigt}}$  by

$$V_S^{\text{Voigt}} = \sqrt{\frac{V_{SH}^2 + 2V_{SV}^2}{3}}, \quad (2)$$

in which  $V_{SH}$  and  $V_{SV}$  are, respectively, the horizontal and vertical shear-wave velocities (Montagner and Anderson, 1989; Chang *et al.*, 2015).

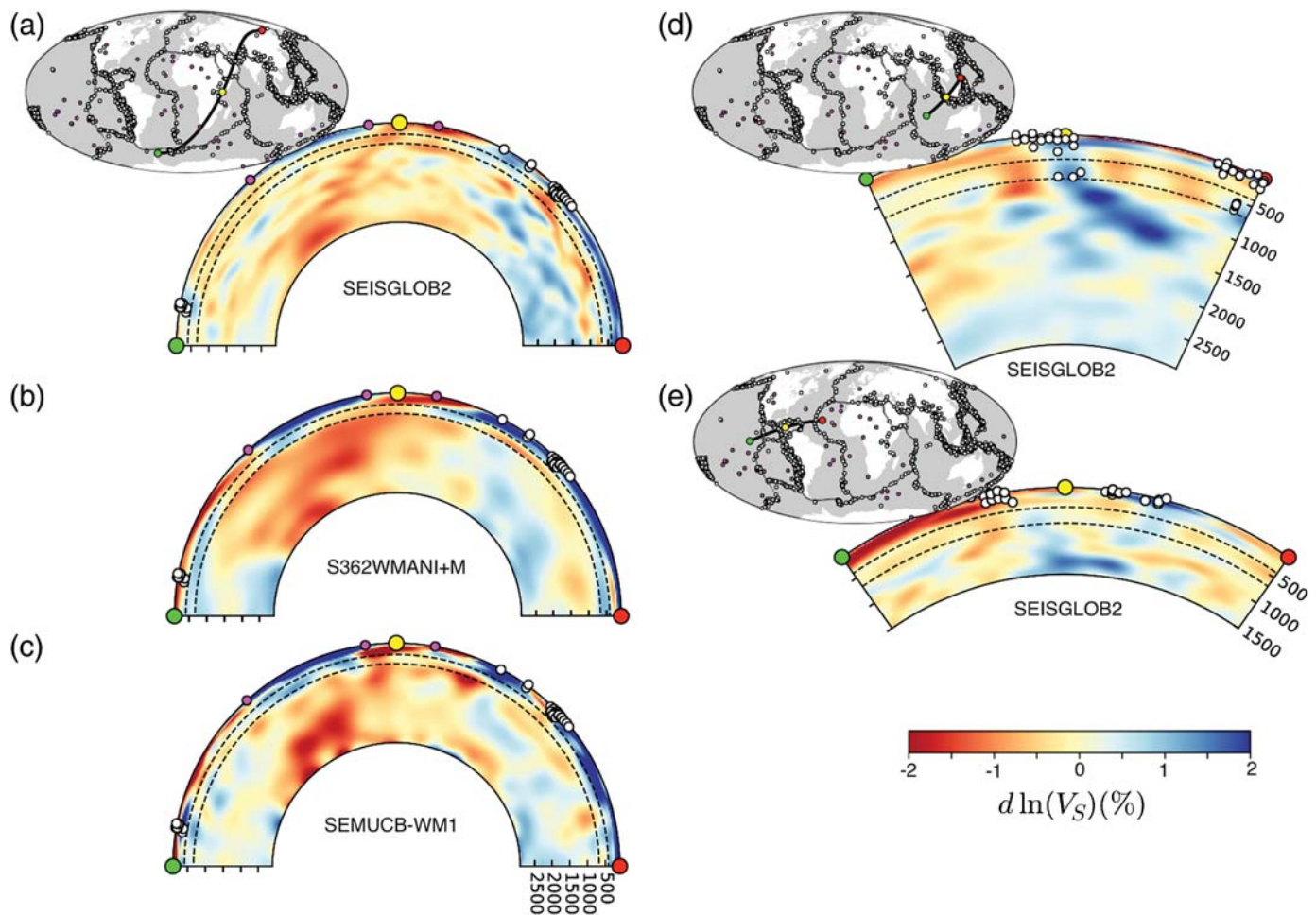
Most of the tomographic models chosen here invert for the shear velocity perturbations  $d \ln(V_S)$  and scale the compressional velocity  $d \ln(V_P)$  and density  $d \ln(\rho)$  perturbations to the shear velocity perturbations, such that  $d \ln(V_P) = \nu_\alpha d \ln(V_S)$  and  $d \ln(\rho) = \nu_\rho d \ln(V_S)$  (see Table 1). The scaling factors  $\nu_\alpha$  and  $\nu_\rho$  can be chosen to be depth independent or depth dependent ( $\nu_\alpha(r)$  and  $\nu_\rho(r)$ ). We took into account the imposed scaling laws by the different authors so that models can be displayed as perturbations of  $V_S$ ,  $V_P$ , or  $\rho$ . The only exception is SP12RTS (Koelemeijer *et al.*, 2016), which provides a  $V_P$  model and we only use  $\nu_\rho$  to build the density model.

We also provide a software package to create the model files so that other models can be uploaded if desired (see section 7 of the documentation available in the © electronic supplement).

**Table 1**  
**Summary of the Characteristics of Every Tomographic Model Included in SeisTomoPy**

<b>Model</b>	<b>Data</b>	<b>Inverted Parameter</b>	<b>Lateral Parameter</b>	<b>Radial Parameter</b>	<b>Theory Used</b>	<b>Reference Model</b>	<b>Scaling Laws</b>	<b>Crustal Model</b>	<b>Global or Upper Mantle</b>
S40RTS (Ritsema <i>et al.</i> , 2011)	SW-phase velocities, BW travel times, NM splitting coefficients	$V_S$	Spherical harmonics up to degree 40	21 cubic spline functions	Ray theory	PREM iso.	$\nu_\alpha$ varies from 2 (surf) to 3 (CMB) $\nu_p = 0.5$	Corrected CRUST2.0 (Bassin <i>et al.</i> , 2000)	Global
S362WMANI +M (Moulik and Ekström, 2014)	SW-phase velocities, Long-period BW waveforms, BW travel times, NM splitting coefficients	$V_{SH}$ , $V_{SV}$	Spherical splines	16 cubic splines discontinuous across 650 km	Ray theory	STW105 (Kustowski <i>et al.</i> , 2008)	$\nu_\alpha = 0.55$ , $\nu_p = 0$	Corrected CRUST2.0	Global
SEMUCB-WM1 (French and Romanowicz, 2014)	SW waveforms ( $T > 60$ s), BW waveforms ( $T > 36$ s and $T > 32$ s)	$V_{SH}$ , $V_{SV}$	Spherical splines	20 cubic spline functions	3D synthetics and NACT	Their own model (French and Romanowicz, 2014)	$\nu_\alpha = 0.5$ , $\nu_p = 0$	Corrected smoothed version CRUST2.0	Global
SGLOBE-rani (Chang <i>et al.</i> , 2015)	SW-phase velocities, BW travel times	$V_{SH}$ , $V_{SV}$	Spherical harmonics up to degree 35	20 cubic spline functions	Ray theory	PREM aniso.	$\nu_\alpha = 0.5$ , $\nu_p = 0.4$	Corrected CRUST2.0	Global
SEISGLOB1 (Durand <i>et al.</i> , 2016)	SW-phase velocities, NM splitting and coupling coefficients	$V_S$	Spherical harmonics up to degree 20	21 cubic spline functions	Ray theory	PREM iso.	$\nu_\alpha = 0.55$ , $\nu_p = 0.2$	Inverted	Global
SPT2RTS (Koelemeijer <i>et al.</i> , 2016)	SW-phase velocities, BW travel times, NM splitting coefficients	$V_S$ , $V_P$	Spherical harmonics up to degree 12	21 cubic spline functions	Ray theory	PREM iso.	$\nu_p = 0.5$	Corrected CRUST2.0	Global
SEISGLOB2 (Durand <i>et al.</i> , 2017)	SW-phase velocities, NM splitting and coupling coefficients	$V_S$	Spherical harmonics up to degree 40	21 cubic spline functions	Ray theory	PREM iso.	$\nu_\alpha = 0.55$ , $\nu_p = 0.2$	Corrected CRUST2.0	Global
3D2016-09S (Debayle <i>et al.</i> , 2016)	SW-phase velocities	$V_{SV}$ , $V_{SH}$	Correlation length 200 down to 750 km increases to 800 down to 1000 km	Correlation length 50 km	Path average	PREM aniso.		Corrected 3SMAC (Nataf and Ricard, 1993)	Upper mantle

CMB, core-mantle boundary; SW, surface waves; BW, body waves; NM, normal modes;  $T$ , period;  $V_S$ ,  $V_P$ ,  $V_{SH}$ ,  $V_{SV}$ , shear velocity, compressional velocity, horizontal shear velocity, and vertical shear velocity;  $\nu_\alpha, \nu_p$ , scaling factors such that  $d \ln(V_p) = \nu_\alpha d \ln(V_S)$  and  $d \ln(\rho) = \nu_p d \ln(V_S)$ .



▲ **Figure 1.** Examples of cross sections obtained in various models (model names below each cross section). Small solid circles show hotspot locations, small white circles denote earthquake locations, and left, middle, and right big solid circles denote the starting, ending, and midpoints, respectively, along the profile. (a–c) Cross sections beneath Africa showing the African large low-shear-velocity province (e.g., Lay *et al.*, 2006; Lay and Garnero, 2011). The profile extends from the surface to the core-mantle boundary and is 180° wide. (d,e) Examples of narrower cross sections and with a smaller depth extent through subduction regions where the location of slab is highlighted by displaying the earthquake location. The color version of this figure is available only in the electronic edition.

### Crustal Considerations

For the models that do not include the crust, the models start beneath the Moho, that is, at 24.4 km for preliminary reference Earth model (PREM; Dziewonski and Anderson, 1981) and STW05 (Kustowski *et al.*, 2008) and 30 km for the reference model of SEMUCB-WM1 (French and Romanowicz, 2014). For the models that include the crust such as SEISGLOB1 (Durand *et al.*, 2016), it is possible to display the model from the surface.

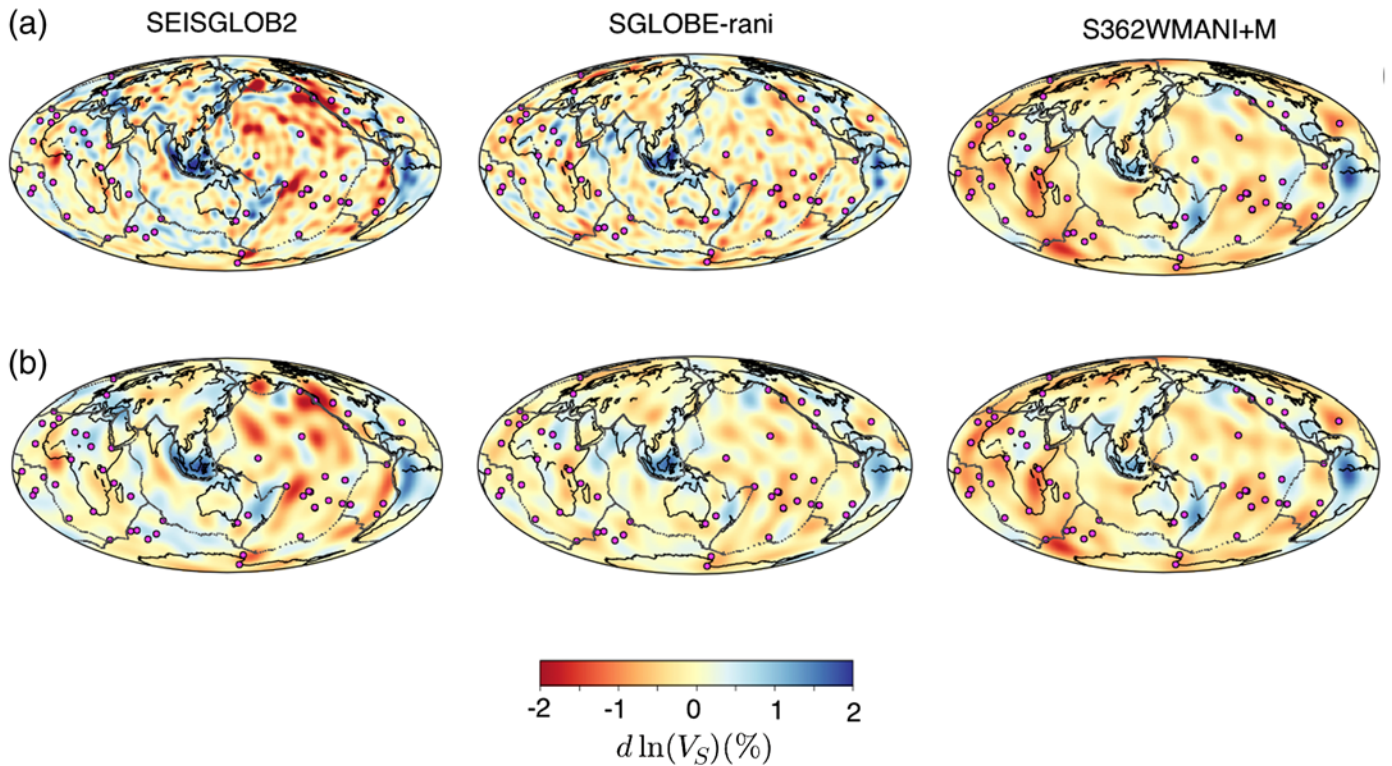
### VISUALIZATION TOOLS: CROSS SECTIONS AND MAPS

The main purpose of these tools is the visual exploration of the various tomographic models.

The user can generate cross sections through  $V_p$ ,  $V_s$ , or density variations anywhere on Earth as illustrated in Figure 1. It can be observed that the 660 km depth discontinuity included in model S362WMANI+M is clearly visible on the cross section

(Fig. 1b) showing that it is properly taken into account in our tool. The model can be displayed up to a chosen spherical harmonic degree up to degree 60. This can be achieved using the graphical interface or by importing `cross_section` and `cross_section_plot` from the `SeisTomoPy` class.

The plate boundaries of model NUVEL-1A (DeMets *et al.*, 1990), the hotspot locations (Müller *et al.*, 1993), and a catalog of earthquakes can be added. This may help position the profile on the region of interest. The catalog of earthquakes is not exhaustive, and it has been built with a minimum of earthquakes such that plate boundaries can be seen. We used events deeper than 100 km depth with magnitudes greater than 5.9 in the 1976–1998 time range and we added all events with magnitudes greater than 5.0 in the 2010–2011 time range. Magnitudes were chosen to be larger than 5.0 to keep the dataset small. The user can also provide their own plate boundary model, hotspot catalog, and earthquake catalog (see section 8 of the documentation available in the © electronic supplement).



▲ **Figure 2.** (a) Examples of maps obtained for three tomographic models (SEISGLOB2, SGLobe-rani, and S362WMANI+M) at 1000 km depth including the first 40 spherical harmonic degrees. Solid circles show hotspot locations and gray lines the plate boundaries. (b) Same as (a) but the models have been filtered down to the spherical harmonic degree 18. The color version of this figure is available only in the electronic edition.

The velocity and density values along the chosen cross sections can be stored as output files, which can then be used for generating synthetic seismograms using AxiSEM (Nissen-Meyer *et al.*, 2014) (see the [An Application of SeisTomoPy to the Study of the Pacific Large Low-Shear-Velocity Province](#) section). It is important to note that AxiSEM is an axisymmetric code that will take the cross section and rotate the structures to arrive at a 3D model. The obtained 3D model is thus not realistic. For more details about AxiSEM, we refer the reader to Nissen-Meyer *et al.* (2014). Our tool also provides files that can be used to visualize wavepaths superimposed on the tomographic model (see the [Calculation Tools: Paths and Travel Times](#) section).

Other than this cross-section tool, we also provide a tool to create maps at a given depth but for the whole globe. Again, the user can either use the graphical interface or import the functions `tomomap` and `tomomap_plot`. We illustrate this tool in Figure 2a. The chosen models have different characteristic wavelengths and for further comparisons it may be useful to display the models with similar length scales, that is, when they are filtered with the same harmonic degree (e.g., Fig. 2a, where we include the first 40 spherical harmonic degrees, whereas in Fig. 2b we chose to keep only degrees smaller than 18).

For details and more examples, see sections 4.1, 4.2, 5.1, and 5.2 of the documentation available in the © electronic supplement.

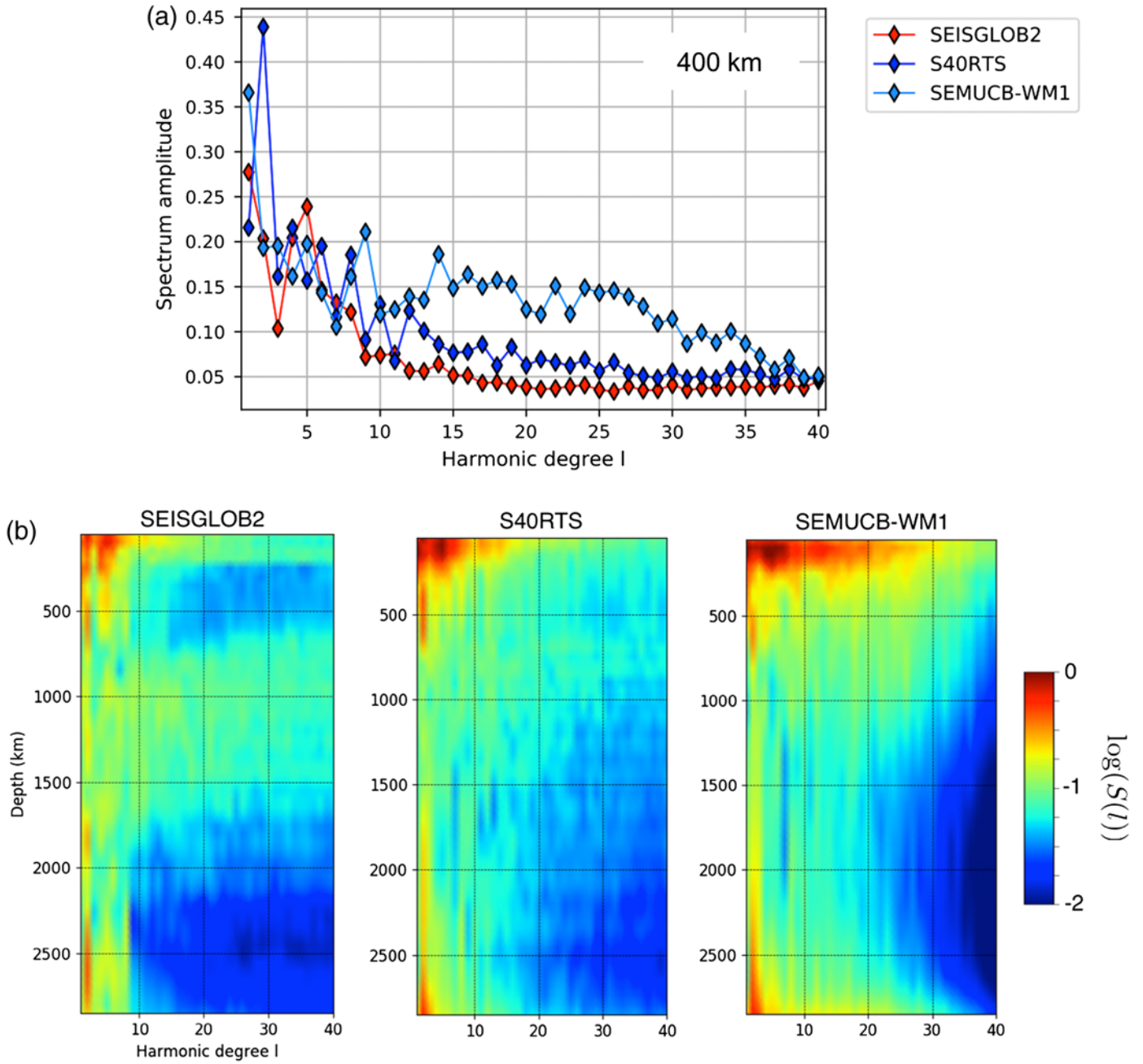
## COMPARISON TOOLS: SPECTRUM AND CORRELATIONS

We added two functions that help the user quantitatively compare different tomographic models. It includes both spectral analysis and correlation analysis.

The user can compute the amplitude spectrum  $S(X, z, l)$  for the different models at a given depth  $z$ , for a given parameter  $X$ , and for a certain spherical harmonic degree  $l$ . It is defined by

$$S(X, z, l) = \sqrt{\frac{1}{4\pi} \sum_{m=-l}^l \left( \frac{\delta X}{X}(z) \right)_{lm} \left( \frac{\delta X}{X}(z) \right)_{lm}^*}, \quad (3)$$

in which the exponent asterisk denotes the complex conjugate and  $\left( \frac{\delta X}{X}(z) \right)_{lm}$  the spherical harmonic coefficients of the considered parameter  $X$  for a given tomographic model at depth  $z$ .  $X$  stands for  $V_S$ ,  $V_P$ , or density. The spectrum gives the importance of each degree in the model and can be used to compare different models (see e.g., Durand *et al.*, 2016) (see Fig. 3a). This tool also allows the user to upload a file with a different model, not included in the suite of models of SeisTomoPy, for a given depth and compute the spectrum of this model. Because of the functions `spectrum` and `spectrum_fromfile` the spectrum calculations can also be run routinely. Figure 3b shows the amplitude spectrum computed



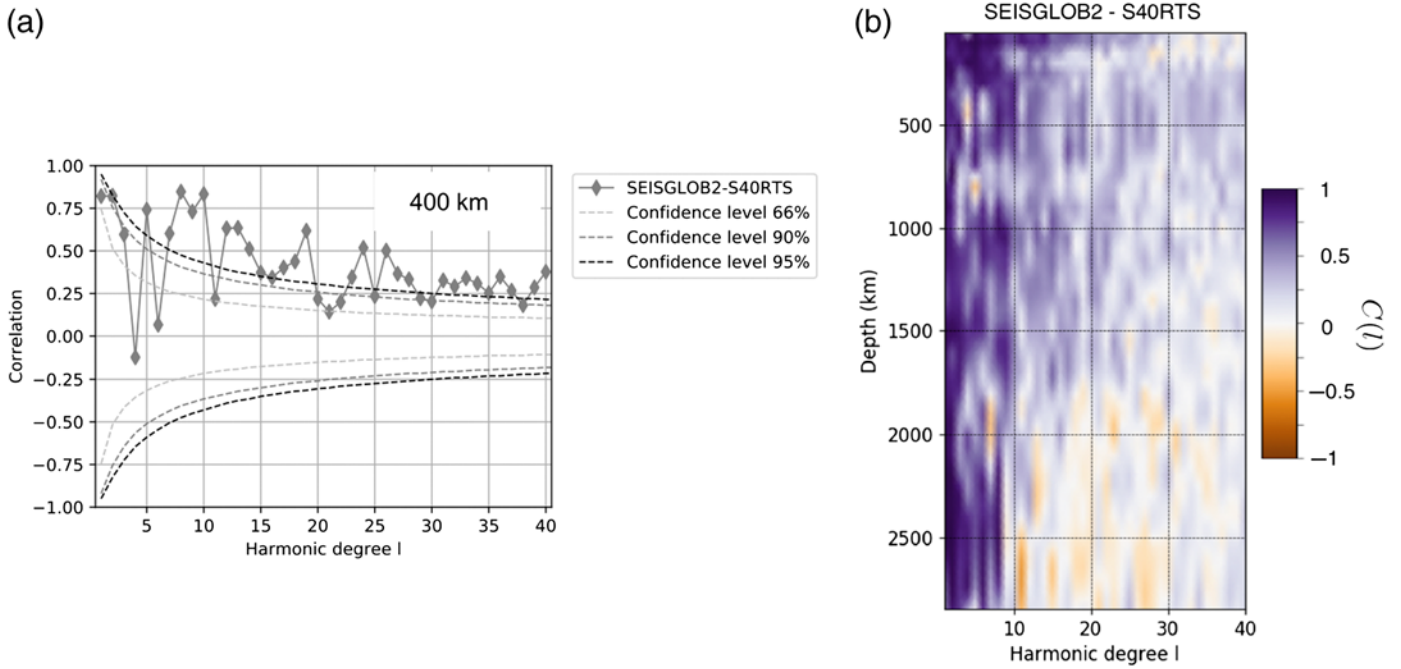
▲ **Figure 3.** (a) Amplitude spectrum of the shear velocity perturbations at 400 km depth for three tomographic models (SEISGLOB2, S40RTS, and SEMUCB-WM1). (b) Same as (a) but repeated at various depths and representing the logarithm of the amplitude spectrum. The color version of this figure is available only in the electronic edition.

with SeisTomoPy for various depths and for three models, SEISGLOB2 (Durand *et al.*, 2017), S40RTS (Ritsema *et al.*, 2011), and SEMUCB-WM1 (French and Romanowicz, 2014).

We then added a tool that enables the user to compute the correlation between two tomographic models 1 and 2. The

correlation can be carried out for any parameter  $X_1$  of model 1 and  $X_2$  of model 2 and for the same depth between the two models ( $z_1 = z_2$ ) or it could be for different depths ( $z_1 \neq z_2$ ). Correlations are then computed at a given spherical harmonic degree  $l$  following:

$$C(X_1, z_1, X_2, z_2, l) = \frac{\sum_{m=-l}^l \left(\frac{\delta X_1}{X_1}(z_1)\right)_{lm} \left(\frac{\delta X_2}{X_2}(z_2)\right)_{lm}^*}{\sqrt{\sum_{m=-l}^l \left(\frac{\delta X_1}{X_1}(z_1)\right)_{lm} \left(\frac{\delta X_1}{X_1}(z_1)\right)_{lm}^* \sum_{m=-l}^l \left(\frac{\delta X_2}{X_2}(z_2)\right)_{lm} \left(\frac{\delta X_2}{X_2}(z_2)\right)_{lm}^*}}. \quad (4)$$



▲ **Figure 4.** (a) Correlation between shear velocity perturbations of model SEISGLOB2 and model S40RTS at 400 km depth with the confidence level curves 66%, 90%, and 95%. (b) Same as (a) but as a function of depth. The color version of this figure is available only in the electronic edition.

As with other correlation methods, equation (4) provides a measure of agreement between the two chosen models: 1 for perfect agreement,  $-1$  for perfect agreement but with opposite sign, and 0 if there is no correlation between the models (see Fig. 4a). The user can again upload their own model to compute the correlation between this model and any other model provided with the tool. The functions `correlation`, `correlation_fromfile`, and `correlation_fromfile2` allow the user to run the correlation calculations routinely. Figure 4b shows examples of correlation functions computed between model SEISGLOB2 (Durand *et al.*, 2017) and S40RTS (Ritsema *et al.*, 2011) as a function of depth.

For details and more examples, see sections 4.3, 4.4, 5.3, and 5.4 of the documentation available in the electronic supplement.

## CALCULATION TOOLS: PATHS AND TRAVEL TIMES

These last two tools allow the user to test which mantle structures are sampled by a certain seismic wave and to compute the associated travel times.

The user can display seismic phases on top of cross sections made in the desired tomographic models. For this, the user must first provide the input file for the cross section, which is either obtained as an output file from the cross-section tool or it can be created by the user for any other model not included in SeisTomoPy. After loading the input file, the cross section is displayed and the user can then additionally load files with event and station locations and a list of seismic phases to

be shown on top of the tomographic image. The user can also run `path_plot` from the SeisTomoPy classes in a terminal without using the graphical interface.

For this tool, we use the wavepaths in the 1D model PREM (Dziewonski and Anderson, 1981) computed using ObsPy-TauP (Crotwell *et al.*, 1999; Beyreuther *et al.*, 2010). This, however, is a sufficient approximation because the velocity perturbations in the mantle are of the order of 1%–2% only, hence the paths are not significantly deviated from the path computed within a 1D reference model such as PREM.

Travel-time delays can also be calculated. They are computed with respect to a reference model through a given tomographic model  $\delta t_{\text{SeisTomoPy}}^{3D}$ , for any given seismic phases and for any combinations of source and receiver provided by the user. To that goal, we compute the paths of the seismic waves using ObsPy-TauP in model PREM and integrate the velocity perturbations of the tomographic model along this path as follows:

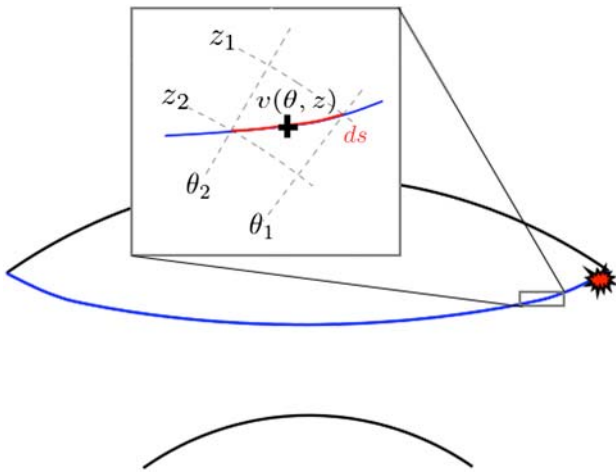
$$\delta t_{\text{SeisTomoPy}}^{3D} = t^{3D} - t^{\text{IDREF}} = - \int_{\text{path}} \frac{\delta V}{V}(\theta, z) \frac{ds(\theta, z)}{V^{3D}(\theta, z)}, \quad (5)$$

in which

$$ds(\theta, z) = \sqrt{z_1^2 + z_2^2 - 2z_1z_2 \cos(\theta_1 - \theta_2)}, \quad (6)$$

in which  $ds$  is the distance along an elementary part of the path, computed in polar coordinates (see Fig. 5), in which  $(z_1, z_2)$ , respectively  $(\theta_1, \theta_2)$ , are the limits of an elementary portion of the path in polar coordinates. We then compute the absolute travel time  $t_{\text{SeisTomoPy}}^{3D}$  by adding the computed travel time in the reference model  $t_{\text{SeisTomoPy}}^{\text{IDREF}}$ , as follows:





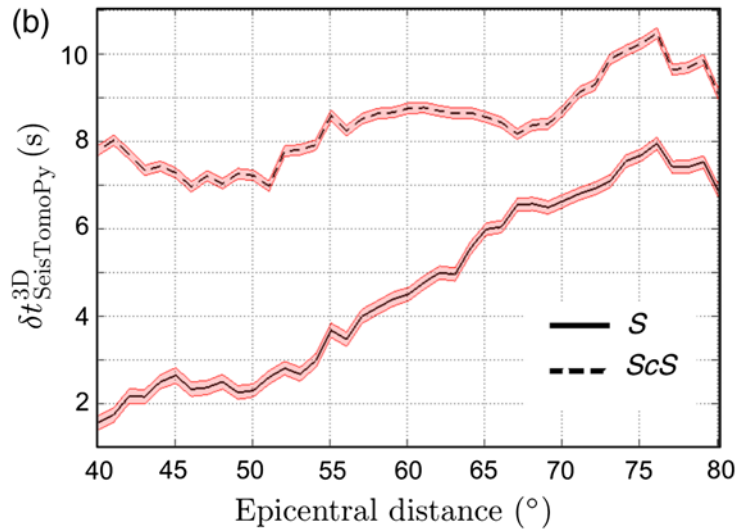
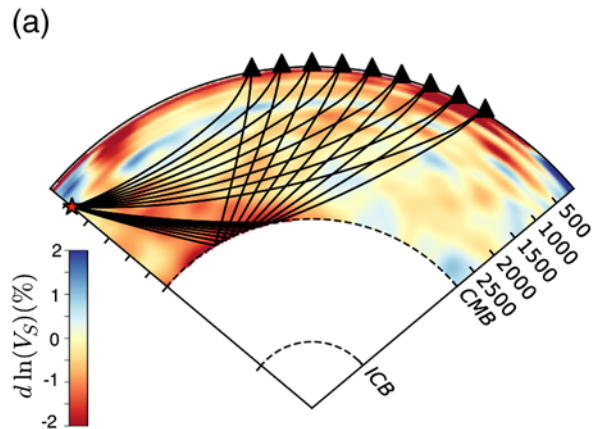
▲ **Figure 5.** Definition of an element of path of length  $ds$  in polar coordinates. The color version of this figure is available only in the electronic edition.

$$t_{\text{SeisTomoPy}}^{\text{3D}} = \delta t_{\text{SeisTomoPy}}^{\text{3D}} + t_{\text{SeisTomoPy}}^{\text{1DREF}} \quad (7)$$

These calculations include the crust only if the tomographic model includes a crustal model, for all other models the user needs to add the effect of the crust. By doing so, the user may choose the best suitable crustal model for their study.

We provide an uncertainty  $\Delta t$  on the computed travel time that represents the precision of the integration. For this, we compute the travel-time integration in the 1D PREM model  $t_{\text{SeisTomoPy}}^{\text{PREM}}$  and compare our result with the output from TauP  $t_{\text{TauP}}^{\text{PREM}}$ , so that

$$\Delta t = \|t_{\text{SeisTomoPy}}^{\text{PREM}} - t_{\text{TauP}}^{\text{PREM}}\|. \quad (8)$$



▲ **Figure 6.** (a) Examples of  $S$  and  $ScS$  ray paths displayed on top of model S40RTS using the paths tool. The region is chosen to include the Pacific low-velocity anomaly. (b) Examples of travel-time delays  $\delta t_{\text{SeisTomoPy}}^{\text{3D}}$ , calculated with SeisTomoPy for  $S$  (solid lines) and  $ScS$  (dashed lines) waves in S40RTS. Shaded areas represent the uncertainties. These travel-time delays only take into account the effect of mantle structures, and the crust effect must be added. The color version of this figure is available only in the electronic edition.

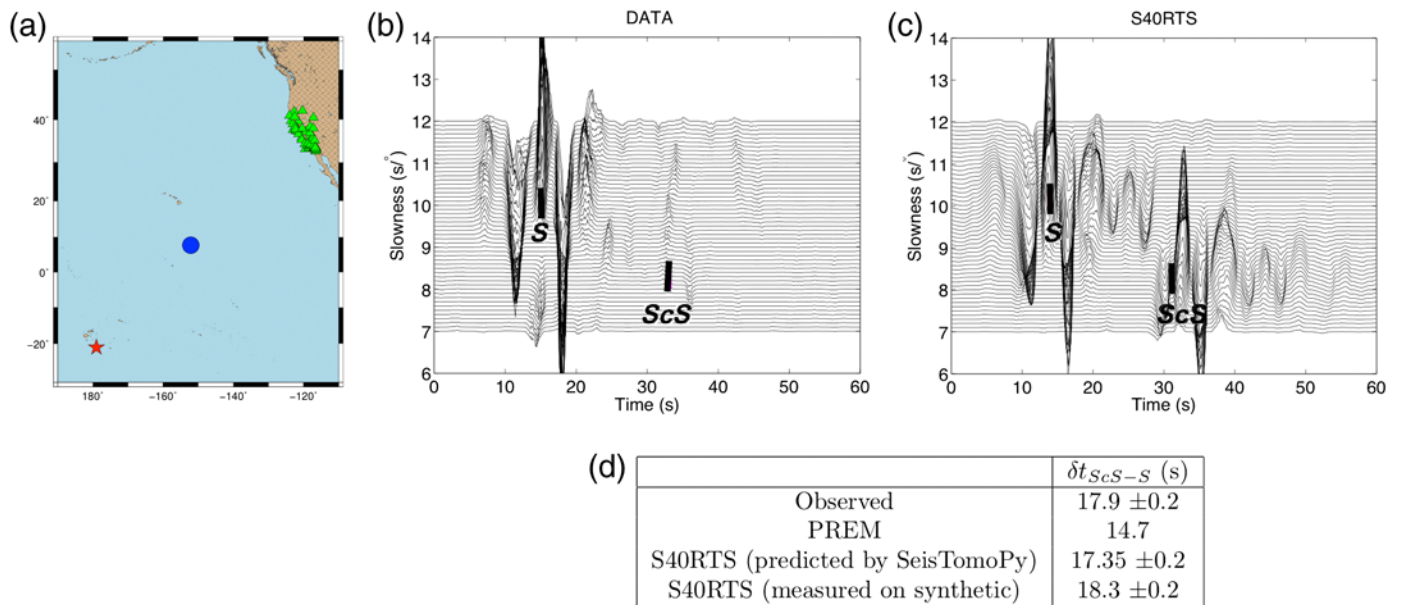
This definition allows us to benchmark our calculations because we verify that we are able to reproduce ObsPy–TauP calculations. We then only impose the velocity perturbations obtained from a given tomographic model to compute the desired travel times.

We illustrate these two tools in Figure 6. We focus here on the Pacific low-velocity anomaly (Lay *et al.*, 2006; Lay and Garnero, 2011) and use direct  $S$  waves and core reflected  $ScS$  waves (see Fig. 6a). We also perform delay time calculations for  $S$  and  $ScS$  waves in the tomographic model S40RTS and display the results in Figure 6b. The delay times  $\delta t_{\text{SeisTomoPy}}^{\text{3D}}$  are given with respect to the reference model (see Table 1 for information on the reference model). The shaded areas show the uncertainties provided by SeisTomoPy. They are very small, of the order of 0.1–0.3 s, here. The delay times are positive, indicating that the waves are slower than in the reference model, as expected for waves propagating through a low-velocity anomaly region.

For details and more examples, see sections 4.5, 4.6, 5.5, and 5.6 of the documentation available in the electronic supplement.

## AN APPLICATION OF SEISTOMOPY TO THE STUDY OF THE PACIFIC LARGE LOW-SHEAR-VELOCITY PROVINCE

In this section, we present an application of SeisTomoPy tools to the imaging of the Pacific low-velocity anomaly. We use an earthquake that occurred on 4 October 2002 recorded at 58 seismic stations across the western United States (see Fig. 7a). The region sampled by this earthquake is illustrated in Figure 6a. The distance between the earthquake and the station is between  $78^\circ$  and  $83^\circ$  which makes the distinction of  $S$  and  $ScS$  waves on a single seismograms difficult because of their close arrival times. We thus apply array seismology methods, namely



**▲ Figure 7.** (a) Map of the 4 October 2022 event (star) and western U.S. stations (triangles). The circle indicates the area of the reflection points of the  $ScS$  waves. (b) Vespagram of the recorded seismograms. Black vertical bars show the picked  $S$  and  $ScS$  waves. (c) Vespagram of the synthetic seismograms. Black vertical bars show the travel times predicted by SeisTomoPy align on the  $S$  signal. (d) Summary of the different  $ScS-S$  differential travel times. The color version of this figure is available only in the electronic edition.

fourth-root vespagrams (see e.g., Rost and Thomas, 2002), to be able to identify the waves and measure  $ScS-S$  delay times.

The vespagram of the data is presented Figure 7b. The black vertical bars show the picked arrival times and theoretical slowness computed in PREM for  $S$  and  $ScS$ . To compare the observations to synthetic data, we then use SeisTomoPy for computing cross sections using the tomographic model S40RTS and use the generated AxiSEM input files to generate synthetic seismograms with AxiSEM (Nissen-Meyer *et al.*, 2014) and Instaseis (van Driel *et al.*, 2015). The vespagram of synthetic traces is displayed in Figure 7c. The predicted travel times for S40RTS by SeisTomoPy are given as black vertical bars and agree with the arrivals of the waves in the vespagram. There is still  $\sim 1$  s of difference that may be attributed to the use of ray theory to compute travel times in SeisTomoPy, while the synthetic seismograms have been computed using 3D wave propagation theory (Nowacki and Wookey, 2016).

We summarize in Figure 7d the various differential travel times. It appears that the calculated travel times of S40RTS using SeisTomoPy are not able to fully explain the measured arrival time of the  $ScS$ . This suggests that the low-velocity region is slower than predicted by S40RTS. Additional structures such as ultra low velocity zone (see e.g., McNamara *et al.*, 2010; Thorne *et al.*, 2013) have been detected in the same area and could cause these travel-time differences.

## ADDING FUNCTIONALITIES

Further functionalities will be added in the future:

- Displaying full anisotropic tomographic models.

- Displaying geodynamic models obtained from modeling codes such as Stag3D (Tackley and Shunxing, 2002), that can then be directly compared with tomographic models.

## CONCLUDING REMARKS

We present SeisTomoPy, a new Python tool, that aims at facilitating the use of tomographic models provided on various web sites and formats, and brought them into a single format to be displayed and compared with other models. SeisTomoPy includes at the moment six tools that provide visualization, comparison, and further calculation facilities to use tomographic models and extract information such as correlations, spectra, and travel times. This tool is freely available on a GitHub platform and will be updated regularly. Through storing many different tomographic models, it can also serve as a library for future tomographic and geodynamic models.

## DATA AND RESOURCES

The Global Centroid Moment Tensor Project database was searched using [www.globalcmt.org/CMTsearch.html](http://www.globalcmt.org/CMTsearch.html) (last accessed November 2017) and the data using Incorporated Research Institutions for Seismology (IRIS) server. For the synthetic seismograms, we used AxiSEM (<http://seis.earth.ox.ac.uk/axisem/>, last accessed November 2017) and Instaseis (<http://www.instaseis.net/>, last accessed November 2017). All the plots were made using Python v.3.6 (<https://www.continuum.io/what-is-anaconda>, last accessed November 2017). All tomographic models used in SeisTomoPy came from published sources listed in the references. SeisTomoPy can be downloaded from

the GitHub platform: <https://github.com/stephaniedurand/SeisTomoPy> (last accessed November 2017). ☒

## ACKNOWLEDGMENTS

This work was supported by the Deutsche Forschungsgemeinschaft (DFG) through the project HAADES DU1634/1-1. The authors thank all the authors of the different tomographic models to provide them to the community. The authors also thank both reviewers for their helpful comments.

## REFERENCES

- Bassin, C., G. Laske, and G. Masters (2000). The current limits of resolution for surface wave tomography in North America, *Eos Trans AGU* **81**, F897.
- Beyreuther, M., R. Barsch, L. Krischer, T. Megies, Y. Behr, and J. Wassermann (2010). ObsPy: A Python toolbox for seismology, *Seismol. Res. Lett.* **81**, no. 3, 530–533.
- Chang, S.-J., A. M. G. Ferreira, J. Ritsema, H. J. van Heijst, and J. H. Woodhouse (2015). Joint inversion for global isotropic and radially anisotropic mantle structure including crustal thickness perturbations, *J. Geophys. Res.* **120**, 4278–4300.
- Crotwell, H. P., T. J. Owens, and J. Ritsema (1999). The TauP toolkit: Flexible seismic travel-time and ray-path utilities, *Seismol. Res. Lett.* **70**, no. 2, 154–160.
- Debayle, E., F. Dubuffet, and S. Durand (2016). An automatically updated S-wave model of the upper mantle and the depth extent of azimuthal anisotropy, *Geophys. Res. Lett.* **43**, no. 2, 674–682.
- DeMets, C., R. Gordon, and D. Argus (1990). Current plate motions, *Geophys. J. Int.* **101**, 425–478.
- Durand, S., E. Debayle, Y. Ricard, and S. Lambotte (2016). Seismic evidence for a change in the large scale tomographic pattern across the D layer, *Geophys. Res. Lett.* **43**, no. 15, 7928–7936.
- Durand, S., E. Debayle, Y. Ricard, C. Zanolli, and S. Lambotte (2017). Confirmation of a change in the global shear velocity pattern at around 1000 km depth, *Geophys. J. Int.* **211**, no. 3, 1628–1639.
- Dziewonski, A. M., and D. L. Anderson (1981). Preliminary reference Earth model, *Phys. Earth Planet. In.* **25**, 297–356.
- Edmonds, A. R. (1960). *Angular and Quantum Mechanics*, Princeton University Press, Princeton, New Jersey.
- French, S. W., and B. Romanowicz (2014). Whole-mantle radially anisotropic shear-velocity structure from spectral-element waveform tomography, *Geophys. J. Int.* **199**, 1303–1327.
- Hutko, A. R., M. Bahavar, C. Trabant, R. T. Weekly, M. Van Fossen, and T. Ahern (2017). Data products at the IRIS-DMC: Growth and usage, *Seismol. Res. Lett.* **88**, no. 3, doi: [10.1785/0220160190](https://doi.org/10.1785/0220160190).
- Incorporated Research Institutions for Seismology Data Management Center (IRIS DMC) (2011). Data services products: EMC, in *A Repository of Earth Models*, doi: [10.17611/DP/EMC.1](https://doi.org/10.17611/DP/EMC.1).
- Koelmeyer, P., J. Ritsema, A. Deuss, and H.-J. Van Heijst (2016). SP12RTS: A degree-12 model of shear- and compressional-wave velocity for Earth's mantle, *Geophys. J. Int.* **204**, no. 2, 1024–1039.
- Kustowski, B., G. Ekstrom, and A. M. Dziewonski (2008). Anisotropic shear-wave velocity structure of the Earth's mantle: A global model, *J. Geophys. Res.* **113**, no. B06306, doi: [10.1029/2007JB005169](https://doi.org/10.1029/2007JB005169).
- Lay, T., and E. Garnero (2011). Deep mantle seismic modeling and imaging, *Annu. Rev. Earth Planet. Sci.* **39**, 91–123.
- Lay, T., J. Hernlund, E. J. Garnero, and M. S. Thorne (2006). A post-perovskite lens and D heat flux beneath the central Pacific, *Science* **314**, 1272–1276.
- Liu, Q., and Y. J. Gu (2012). Seismic imaging: From classical to adjoint tomography, *Tectonophysics* **566/567**, 31–66.
- Montagner, J.-P., and D. Anderson (1989). Petrological constraints on seismic anisotropy, *Phys. Earth Planet. In.* **54**, 82–105.
- Mosca, I., and J. Trampert (2009). Path-average kernels for long wavelength traveltime tomography, *Geophys. J. Int.* **177**, 639–650.
- Moulik, P., and G. Ekström (2014). An anisotropic shear velocity model of the Earth's mantle using normal modes, body waves, surface waves and long-period waveforms, *Geophys. J. Int.* **193**, 1713–1738.
- Müller, R. D., J.-Y. Royer, and L. A. Lawver (1993). Revised plate motions relative to the hotspots from combined Atlantic and Indian Ocean hotspot tracks, *Geology* **21**, 275–278.
- McNamara, A.-K., E. J. Garnero, and S. Rost (2010). Tracking deep mantle reservoirs with ultra-low velocity zones, *Earth Planet. Sci. Lett.* **299**, 1–9.
- Nataf, H., and Y. Ricard (1993). 3SMAC: An a priori tomographic model of the upper mantle based on geophysical modeling, *Phys. Earth Planet. In.* **95**, 101–122.
- Nissen-Meyer, T., M. van Driel, S. C. Stähler, K. Hosseini, S. Hempel, L. Auer, A. Colombi, and A. Fournier (2014). AxiSEM: Broadband 3-D seismic wavefields in axisymmetric media, *Solid Earth* **5**, 425–445.
- Nolet, G. (1990). Partitioned waveform inversion and two-dimensional structure under the network of autonomously recording seismographs, *J. Geophys. Res.* **95**, 8499–8512.
- Nowacki, A., and J. Wookey (2016). The limits of ray theory when measuring shear wave splitting in the lowermost mantle with ScS waves, *Geophys. J. Int.* **207**, 1573–1583.
- Ritsema, J., A. Deuss, H. J. van Heijst, and J. H. Woodhouse (2011). S40RTS: A degree-40 shear-velocity model for the mantle from new Rayleigh wave dispersion, teleseismic traveltimes and normal-mode splitting function measurements, *Geophys. J. Int.* **184**, 1223–1236.
- Romanowicz, B. (2003). Global mantle tomography: Progress status in the past 10 years, *Annu. Rev. Earth Planet. Sci.* **31**, 303–328.
- Rost, S., and C. Thomas (2002). Array seismology: Methods and applications, *Rev. Geophys.* **40**, no. 3, 2–26.
- Schmerr, N., and E. Garnero (2006). Investigation of upper mantle discontinuity structure beneath the central Pacific using SS precursors, *J. Geophys. Res.* **111**, no. B08305, 1–21.
- Simmons, N. A., S. C. Myers, G. Johannesson, E. Matzel, and S. P. Grand (2015). Evidence for long-lived subduction of an ancient tectonic plate beneath the southern Indian Ocean, *Geophys. Res. Lett.* **42**, 1–9.
- Stutzmann, E., and J. P. Montagner (1993). An inverse technique for retrieving higher mode phase velocity and mantle structure, *Geophys. J. Int.* **113**, 669–683.
- Tackley, P., and X. Shunxing (2002). The thermochemical structure and evolution of Earth's mantle: Constraints and numerical models, *Phil. Trans. Roy. Soc. Lond. A* **360**, no. 1800, 2593–2609.
- Thorne, M., Y. Zhang, and J. Ritsema (2013). Evaluation of 1D and 3D seismic models of the Pacific lower mantle with S, SKS, and SKS traveltimes and amplitudes, *J. Geophys. Res.* **118**, 985–995.
- van Driel, M., L. Krischer, S. C. Stähler, K. Hosseini, and T. Nissen-Meyer (2015). Instaseis: Instant global seismograms based on a broadband waveform database, *Solid Earth* **6**, 701–717.

S. Durand  
R. Abreu  
C. Thomas  
Institut für Geophysik  
Corrensstraße 24  
48149 Münster  
Germany  
[durand@uni-muenster.de](mailto:durand@uni-muenster.de)  
[abreu@uni-muenster.de](mailto:abreu@uni-muenster.de)  
[tine@earth.uni-muenster.de](mailto:tine@earth.uni-muenster.de)

Published Online 10 January 2018